### Title

Overcoming Metastable CO2 Adsorption in a Bulky Diamine-Appended Metal–Organic Framework




### Journal

Journal of the American Chemical Society, 143(37)

### ISSN

0002-7863



### Authors

Dinakar, Bhavish
Forse, Alexander C
Jiang, Henry ZH
et al.



### Publication Date

2021-09-22

### DOI

10.1021/jacs.1c06434

Peer reviewed

# Overcoming Metastable $CO_2$ Adsorption in a Bulky Diamine-Appended Metal–Organic Framework

Bhavish Dinakar,[a,b] Alexander C. Forse,[a,c,d] Henry Z. H. Jiang,[a,b] Ziting Zhu,[b,e] Jung-Hoon Lee,[f] Eugene J. Kim,[c] Surya T. Parker,[a,b] Connor J. Pollak,[a] Rebecca L. Siegelman,[b,c,#] Phillip J. Milner,[b,c,$] Jeffrey A. Reimer,*[a,b] Jeffrey R. Long*[a,b,c]

[a] Department of Chemical and Biomolecular Engineering, University of California, Berkeley, California 94720, United States

[b] Materials Sciences Division, Lawrence Berkeley National Laboratory, Berkeley, California 94720, United States

[c] Department of Chemistry, University of California, Berkeley, California 94720, United States

[d] Department of Chemistry, University of Cambridge, Cambridge, CB2 1EW, U.K.

[e] Department of Materials Science and Engineering, University of California, Berkeley, California 94720, United States

[f] Computational Science Research Center, Korea Institute of Science and Technology (KIST), Seoul 02792, Republic of Korea

*Correspondence to Jeffrey R. Long: jrlong@berkeley.edu and Jeffrey A. Reimer: reimer@berkeley.edu

**ABSTRACT:** Carbon capture at fossil fuel-fired power plants is a critical strategy to mitigate anthropogenic contributions to global warming, but widespread deployment of this technology is hindered by a lack of energy-efficient materials that can be optimized for $CO_2$ capture from a specific flue gas. As a result of their tunable, step-shaped $CO_2$ adsorption profiles, diamine-functionalized metal–organic frameworks (MOFs) of the form diamine–$Mg_2$(dobpdc) (dobpdc$^{4-}$ = 4,4′-dioxidobiphenyl-3,3′-dicarboxylate) are among the most promising materials for carbon capture applications. Here, we present a detailed investigation of dmen–$Mg_2$(dobpdc) (dmen = 1,2-diamino-2-methylpropane), one of only two MOFs with an adsorption step near the optimal pressure for $CO_2$ capture from coal flue gas. While prior characterization suggested that this material only adsorbs $CO_2$ to half capacity (0.5 $CO_2$ per diamine) at 1 bar, we show that the half-capacity state is actually a metastable intermediate. Under appropriate conditions, the MOF adsorbs $CO_2$ to full capacity, but conversion from the half-capacity structure happens on a very slow timescale, rendering it inaccessible in traditional adsorption measurements. Data from solid-state magic angle spinning nuclear magnetic resonance spectroscopy, coupled with van der Waals-corrected density functional theory, indicate that ammonium carbamate chains formed at half- and full-capacity adopt opposing configurations, and the need to convert between these states likely dictates the sluggish post-half capacity uptake. Using the more symmetric parent framework $Mg_2$(pc-dobpdc) (pc-dobpdc$^{4-}$ = 3,3′-dioxidobiphenyl-4,4′-dicarboxylate), the metastable trap can be avoided and the full $CO_2$ capacity of dmen–$Mg_2$(pc-dobpdc) accessed under conditions relevant for carbon capture from coal-fired power plants.

## INTRODUCTION

Anthropogenic $CO_2$ emissions from fossil fuel combustion are driving global warming at a rate of 0.2 °C per decade,[1] and a substantial two-thirds of these emissions derive from the power sector alone.[2] Even as we transition to renewable energy sources in a critical thrust toward sustainability, the burning of fossil fuels is projected to continue for several decades. It is therefore essential to identify strategies for mitigating $CO_2$ emissions in the short term.[3] Additionally, industrial cement and steel plants produce $CO_2$ as a byproduct of mineral conversion, which cannot be avoided by using renewable energy sources.[4,5] Carbon capture and sequestration (CCS) is a potential mitigation strategy wherein $CO_2$ is removed from point sources of production and injected underground for long-term storage.[6] Current state-of-the-art carbon capture technologies rely on aqueous amine solutions that selectively absorb $CO_2$ to form ammonium carbamate and ammonium bicarbonate species.[7] However, these solutions suffer from significant drawbacks, including amine volatilization, thermal and oxidative degradation, and low $CO_2$ adsorption capacities, the latter due to the high water content required to prevent equipment corrosion.[8] Critically, the high energy cost needed to heat the amine solutions to desorb $CO_2$ can reduce power plant output by 20–30%.[9] As a result, energy-efficient $CO_2$ separation materials with high selectivities and capacities are needed to catalyze the widespread implementation of CCS.[9]

Among the most promising materials studied to date for carbon capture are metal–organic frameworks (MOFs). Composed of metal ions or clusters connected by organic linkers, these porous adsorbents possess large internal surface areas, low heat capacities, and are chemically and thermally robust.[10] In particular, materials featuring diamines tethered to the coordinatively-unsaturated metal sites in $Mg_2$(dobpdc) (dobpdc$^{4-}$ = 4,4′-dioxidobiphenyl-3,3′-dicarboxylate) (Figure 1a) have emerged as top performing materials for a range of $CO_2$ separation applications.[11–19] These frameworks exhibit step-shaped $CO_2$ adsorption, which is associated with sudden uptake of one molecule of $CO_2$ per diamine (hereafter referred to as full capacity) at a critical threshold pressure. This unique adsorption behavior originates from a cooperative chemisorption mechanism wherein

$CO_2$ inserts into the metal–diamine bonds to form chains of ammonium carbamate that run along the framework channels (Figure 1b).[12,20] Importantly, these materials exhibit large working capacities with only moderate temperature and/or pressure swings, and the critical pressure or temperature threshold of cooperative adsorption can be controlled by altering the appended diamine,[13–15,17–19] metal,[12,15] and organic linker.[16] A statistical mechanical model in tandem with van der Waals-corrected density functional theory (vdW-DFT) has suggested that cooperative $CO_2$ uptake in diamine–$Mg_2$(dobpdc) is induced by an abrupt increase in the mean ammonium carbamate chain length above a certain pressure of $CO_2$.[21] Recently, this class of materials has been extended to include tetraamine-appended variants of $Mg_2$(dobpdc), which exhibit exceptional cycling stability under humid conditions and with steam regeneration.[22]

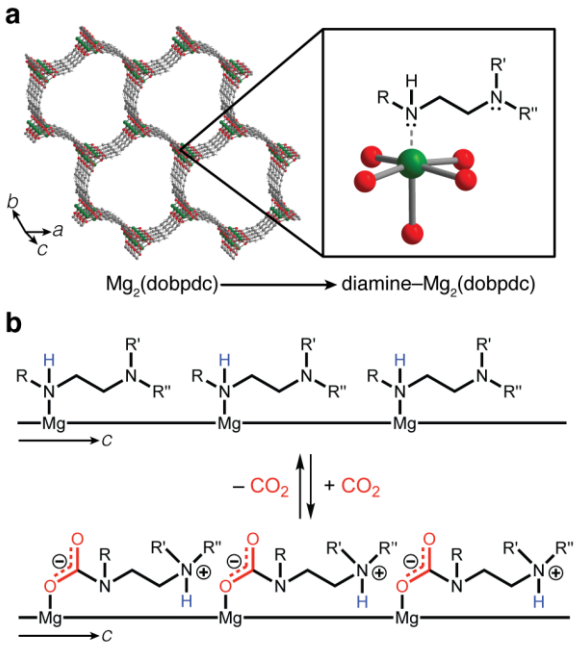


**Figure 1.** (a) Structure of activated $Mg_2$(dobpdc) and expanded view of the coordinatively unsaturated metal sites, which can be post-synthetically functionalized with diamines to access diamine–$Mg_2$(dobpdc). Green, red, gray, and white depict Mg, O, C, and H atoms, respectively. (b) Depiction of the formation of ammonium carbamate chains in diamine–$Mg_2$(dobpdc) upon cooperative $CO_2$ adsorption.

One potential application for diamine-appended MOFs is post-combustion carbon capture from coal-fired power plants, which are responsible for 30% of global anthropogenic $CO_2$ emissions.[2] A typical coal flue gas is composed of $N_2$ (70–75%), $CO_2$ (15–16%), $H_2O$ (5–7%), $O_2$ (3–4%), as well as trace amounts of $SO_x$, $NO_x$, HCl, CO, and hydrocarbons, and is released at ambient pressures and temperatures as low as 40 °C.[23] Therefore, to achieve a target $CO_2$ capture fraction of at least 90% with minimal required regeneration energy, a suitable cooperative adsorbent will exhibit a step pressure of 15 mbar at 40 °C.[13,15] While most diamine–$Mg_2$(dobpdc) materials studied to date display isotherm step pressures of less than 1 mbar or greater than 100 mbar, the frameworks dmpn–$Mg_2$(dobpdc) and dmen–$Mg_2$(dobpdc) (dmpn = 2,2-dimethyl-1,3-propanediamine; dmen = 1,2-diamino-2-methylpropane)[15] both exhibit intermediate step pressures close to the ideal pressure of 15 mbar at 40 °C suitable for energy-efficient $CO_2$ capture from coal flue gas. The working capacity of dmpn–$Mg_2$(dobpdc) is 2.42 mmol/g (10.7 g/100g) with a 60 °C temperature swing, and the material can be regenerated under humid $CO_2$ at ambient pressures.[15] However, dmpn–$Mg_2$(dobpdc) adsorbs $CO_2$ through a mixed adsorption mechanism involving gradual equilibration to a 1:1 ratio of ammonium carbamate chains and hydrogen-bonded carbamic acid pairs. As a result, the $CO_2$ cycling capacity of this material is significantly lower than the theoretical capacity predicted from the formation of ammonium carbamate chains alone.[24] The related framework material dmen–$Mg_2$(dobpdc) has likewise been reported to exhibit an unusual adsorption profile under isobaric and isothermal conditions.[15,17] For example, isothermal data collected at 40 °C revealed a single sharp adsorption step to approximately half capacity (2.5 mmol/g, corresponding to slightly more than 0.5 $CO_2$/dmen), with minimal and gradual post-step adsorption indicative of $CO_2$ physisorption.[15,17] Preliminary isobaric data collected using a temperature ramp rate of 1 °C/min likewise revealed stepped adsorption to an apparent maximum capacity of ~0.5 $CO_2$/dmen at 40 °C.[15]

We were interested in understanding the mechanism of $CO_2$ uptake in dmen–$Mg_2$(dobpdc) and identifying the cause of this unusual adsorption behavior, which precludes its adoption for $CO_2$ capture from coal flue gas, despite its ideal step pressure, high recyclability, and stability to $O_2$, $H_2O$, and $SO_2$.[17] Here, we show that that by carefully controlling the $CO_2$ dosing method, it is possible to access the full capacity (1 $CO_2$/dmen) of dmen–$Mg_2$(dobpdc) at 1 bar of $CO_2$. Unexpectedly, the half-capacity structure represents a metastable trap that has not been encountered with any other diamine-appended $Mg_2$(dobpdc) material studied to date. Characterization of the half- and full-capacity structures using solid-state nuclear magnetic resonance (NMR) spectroscopy and vdW-DFT reveals the existence of a preferred ammonium carbamate chain direction in each case, likely dictated by steric interactions and favorable non-covalent interactions. By changing the base framework, it is possible to avoid the half-capacity trap, yielding a material that readily saturates with $CO_2$ under conditions relevant to capture from a coal flue gas.

## RESULTS AND DISCUSSION

**Uptake of $CO_2$ in dmen–$Mg_2$(dobpdc).** New $CO_2$ adsorption data were collected for dmen–$Mg_2$(dobpdc) and compared with new data collected for the well-characterized frameworks e-2–$Mg_2$(dobpdc) (e-2 = *N*-ethylethylenediamine)[13] and *n*Pr-2–$Mg_2$(dobpdc) (*n*Pr-2 = *N*-propylethylenediamine).[16] These reference materials have previously been shown to adsorb $CO_2$ to full capacity via the exclusive formation of ammonium carbamate chains, as characterized via detailed solid-state NMR studies.[23] All materials were prepared and activated using a reported procedure,[15] and optimal diamine loadings of 100% were achieved within error (Supporting Information, Table S1). Carbon dioxide adsorption isobars were obtained for all three frameworks using thermogravimetric analysis (TGA) (Figure 2a). The $CO_2$ adsorption isobar of e-2–$Mg_2$(dobpdc) features a single adsorption step to full capacity (Figure 2a),[13,24] while the isobar of *n*Pr-2–$Mg_2$(dobpdc) features a double step, with each step corresponding to half of the theoretical adsorption capacity. For both materials, the experimental capacities (Table S1) are consistent with those in the literature.[13,16] As previously reported, the two steps observed for *n*Pr-2–$Mg_2$(dobpdc) (and related variants with *primary,secondary* alkylethylenediamines featuring bulky secondary amine substituents) suggest that the material cooperatively adsorbs $CO_2$ in two stages, likely due to

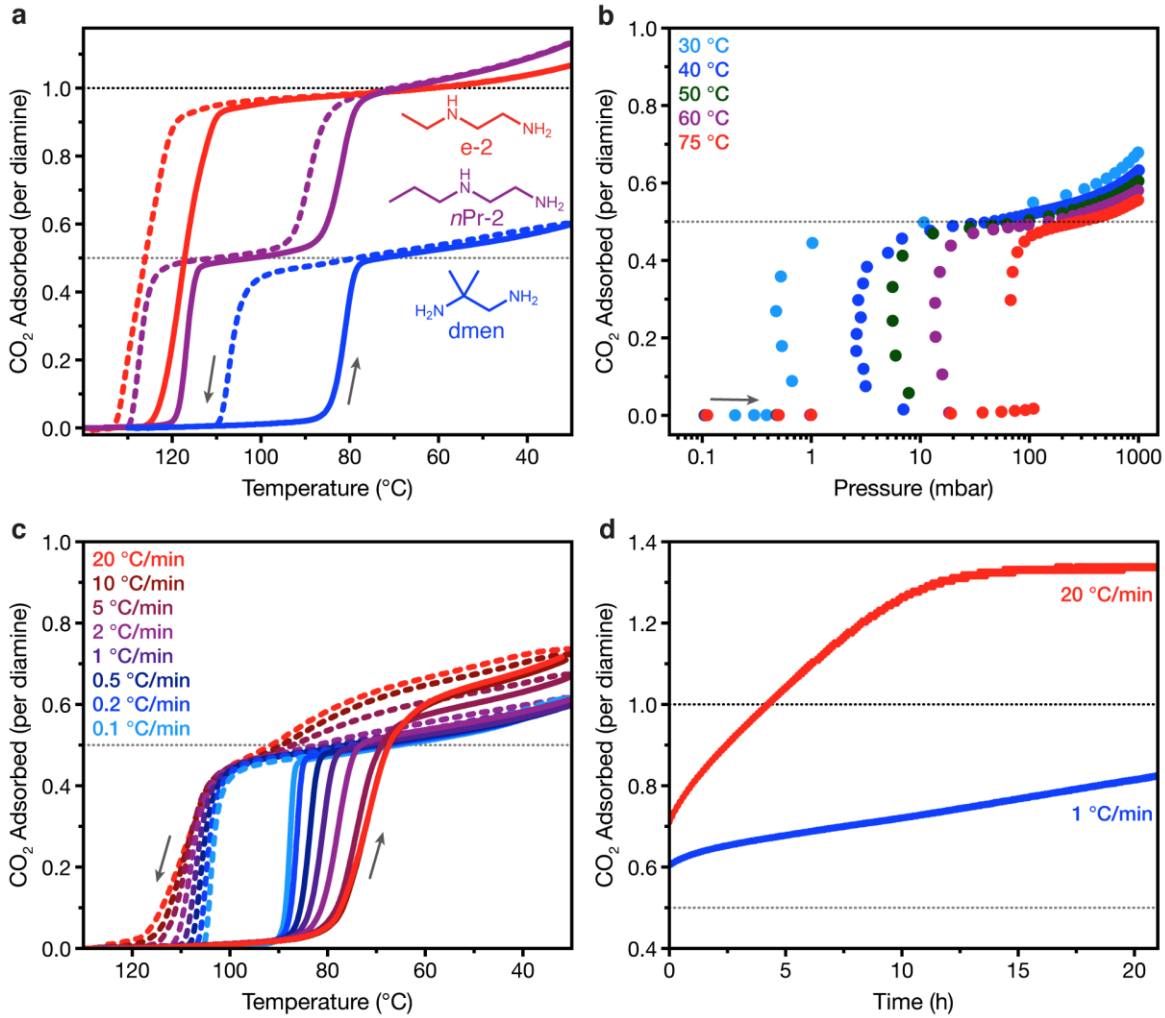


**Figure 2.** (a) Thermogravimetric isobars obtained for e-2–$Mg_2$(dobpdc) (red), *n*Pr-2–$Mg_2$(dobpdc) (purple), and dmen–$Mg_2$(dobpdc) (blue) under an atmosphere of pure $CO_2$ using a temperature ramp rate of 1 °C/min. Adsorption and desorption curves are shown as solid and dashed lines, respectively. The samples were held isothermally at 30 °C for 5 min before desorption data were collected to allow the temperature to equilibrate. (b) Pure $CO_2$ adsorption isotherms for dmen–$Mg_2$(dobpdc) at various temperatures. The apparent decrease in pressure with increasing loading in the step region at low temperatures is not fully understood; however, it is a phenomenon that has been observed previously for diamine-appended MOFs[14,16] and may arise due to the nature of how $CO_2$ is dosed in adsorption isotherms (see Ref. 25 for a statistical mechanical analysis of a relevant model scenario). (c) Isobars of dmen–$Mg_2$(dobpdc) under an atmosphere of pure $CO_2$ using the indicated temperature ramp rates. Adsorption and desorption isobars are shown using solid and dashed lines, respectively. Gray arrows indicate the direction of temperature change. (d) Time-dependent $CO_2$ uptake in dmen–$Mg_2$ (dobpdc) at 30 °C after isobars were obtained with ramp rates of 1 and 20 °C/min. Gray and black dashed lines indicate capacities of 0.5 $CO_2$ per diamine (half capacity) and 1 $CO_2$ per diamine (full capacity), respectively. For dmen–$Mg_2$(dobpdc), 1 $CO_2$ per diamine is 4.0 mmol/g, or 17.8 g/100g.

steric interactions between the propyl groups in the crystallographic *ab* plane.[16] As expected, differential scanning calorimetry (DSC) curves collected for e-2–$Mg_2$(dobpdc) and *n*Pr-2–$Mg_2$(dobpdc) are characterized by one and two sharp $CO_2$ adsorption exotherms, respectively (Figure S5). In contrast, the isobar of dmen–$Mg_2$(dobpdc) features only a single step to approximately half of the theoretical capacity at the lowest measured temperature of 30 °C (Figure 2a, Table S1), consistent with prior characterization of $CO_2$ uptake in this material.[15,17] Furthermore, there is only one peak in the DSC curve from 140 to −60 °C, indicating that no additional adsorption step takes place after the step to half capacity (Figures S5 and S6).

Volumetric adsorption isotherms were collected to further investigate the $CO_2$ adsorption behavior of dmen–$Mg_2$(dobpdc) (Figure 2b). This measurement technique is designed to obtain equilibrated data, as defined by a pressure change of less than 0.01% over an average of 11 consecutive user-specified time intervals (here, 30 s). Similar to the isobar data, the adsorption isotherms feature a sharp step to half capacity (0.5 $CO_2$/dmen), followed by only minor subsequent adsorption. This behavior stands in contrast with all other reported materials in the diamine–$Mg_2$(dobpdc) family, in which the full chemisorption capacity can be accessed upon reaching sufficiently low temperatures or high pressures.[13–19,26]

Additional isobar data were collected for dmen–$Mg_2$(dobpdc) using temperature ramp rates between 0.1 and 20 °C/min (Figure 2c). Under ramp rates less than or equal to 1 °C/min, the material adsorbed $CO_2$ to just slightly above half capacity, consistent with previous preliminary data collected for the material at a ramp rate of 1 °C/min.[15] However, the use of faster ramp rates resulted in an unexpected increase in $CO_2$ uptake. For example, at the fastest achievable ramp rate of 20 °C/min, the material adsorbed 0.70 $CO_2$ per diamine (12.4 g/100 g) at 30 °C, compared with 0.60 $CO_2$ per diamine (10.7 g/100 g) at the same temperature with a ramp rate of 1 °C/min. In contrast, the adsorption capacities of e-2–$Mg_2$(dobpdc) and *n*Pr-2–

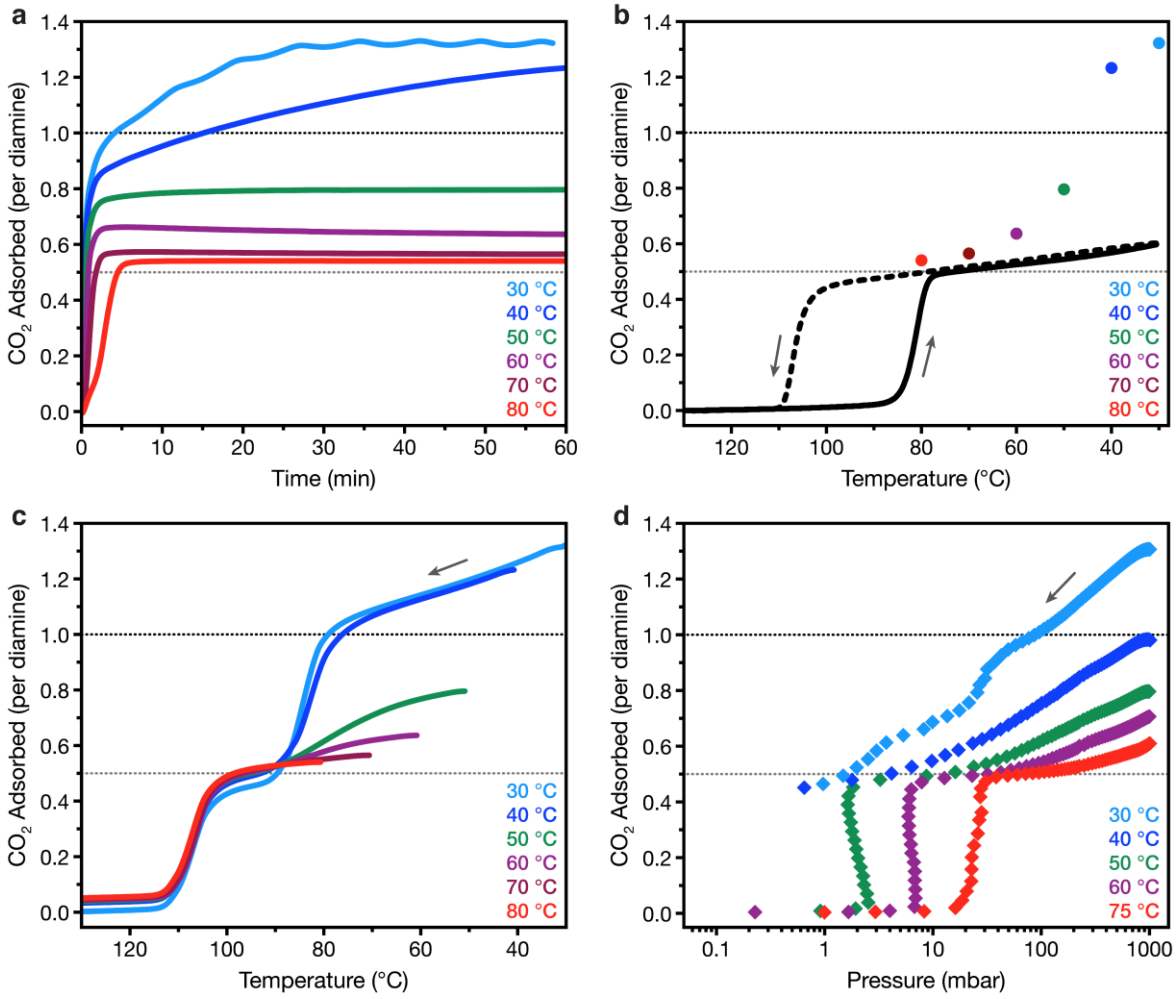


**Figure 3.** $CO_2$ adsorption and desorption in dmen–$Mg_2$(dobpdc). (a) $CO_2$ adsorption kinetics profiles at various temperatures obtained from TGA. For each data set, the activated sample was cooled to the temperature of interest at atmospheric pressure under flowing $N_2$ and then dosed with flowing $CO_2$ at 1 bar and held isothermally for 1 h. The oscillations at 30 °C are due to temperature fluctuations resulting from the TGA operating close to room temperature. (b) Overlay of the 1 °C/min adsorption/desorption isobars (solid and dashed lines, respectively) with the equilibrium adsorption capacities determined from the adsorption profiles in (a) (colored symbols). (c) $CO_2$ desorption isobars collected under an atmosphere of pure $CO_2$ with a ramp rate of 1 °C/min, starting from the equilibrated configuration at various temperatures as shown in (a). (d) Shock–desorption isotherms at various temperatures, with diamonds representing desorption data. Gray arrows indicate the direction of temperature or pressure change. Gray and black dashed lines indicate capacities of 0.5 $CO_2$ per diamine (half capacity) and 1 $CO_2$ per diamine (full capacity), respectively.

$Mg_2$(dobpdc) were not affected by changes in the temperature ramp rate (Figures S1 and S2). Notably, holding a sample of dmen–$Mg_2$(dobpdc) at 30 °C after collecting the 20 °C/min adsorption isobar resulted in additional slow uptake of $CO_2$ that stabilized at ~1.3 $CO_2$ per diamine after ~15 h (Figure 2d, red data). Additional uptake was also observed when holding the sample at 30 °C after collecting an isobar with a 1 °C/min ramp rate, albeit at a much slower rate than for the 20 °C/min data (Figure 2d, blue data). After 21 h, the material had adsorbed only ~0.8 $CO_2$ per diamine. These results suggest that at 30 °C, the equilibrium capacity of dmen–$Mg_2$(dobpdc) is much higher than that accessible from typical isobar and isotherm experiments (Figure 2a and b).

To further investigate this unusual sluggish adsorption behavior, kinetics data were collected using TGA after dosing activated dmen–$Mg_2$(dobpdc) with 1 bar of pure $CO_2$ at various temperatures (Figure 3a).[27] Surprisingly, $CO_2$ uptake in dmen–$Mg_2$(dobpdc) at 30 °C is fairly rapid. After five min, the material adsorbs ~1 $CO_2$ per diamine, and the uptake then plateaus at a capacity of 1.3 $CO_2$ per diamine after only ~35 min. At 40 °C, the quantity of $CO_2$ adsorbed is ~1.2 $CO_2$ per diamine, which continues increasing after an hour. At 50, 60, 70, and 80 °C, the $CO_2$ uptake plateaus in under 5 min at values less than 0.8 $CO_2$ per diamine. We hypothesize that the endpoints of the adsorption curves in Figure 3a correspond to the equilibrium capacities of the material at the respective temperatures, and that the slow ramp rate isobars (Figure 2c) indicate the formation of a metastable intermediate, which slowly converts to the full-capacity state of the material (1 $CO_2$ per diamine), with some additional $CO_2$ physisorption. When the equilibrium capacities from these experiments are overlaid with the original 1 °C/min isobar from Figure 3a, it is clear that the isobar does not reflect the equilibrium adsorption capacity for temperatures below 70 °C (Figure 3b).

To investigate the discrepancy between the kinetics profiles and the slow-ramp adsorption data, we used TGA to measure the *desorption* of $CO_2$ from the adsorbed, equilibrated states, rather than *adsorption* starting from the activated material. After the equilibrated states were achieved at the end of the adsorption kinetics experiments (Figure 3a), the gas flow was changed from $CO_2$ to $N_2$ and the sample was held under flowing $N_2$ for 1 h at each temperature of interest (Figure S10). At 30

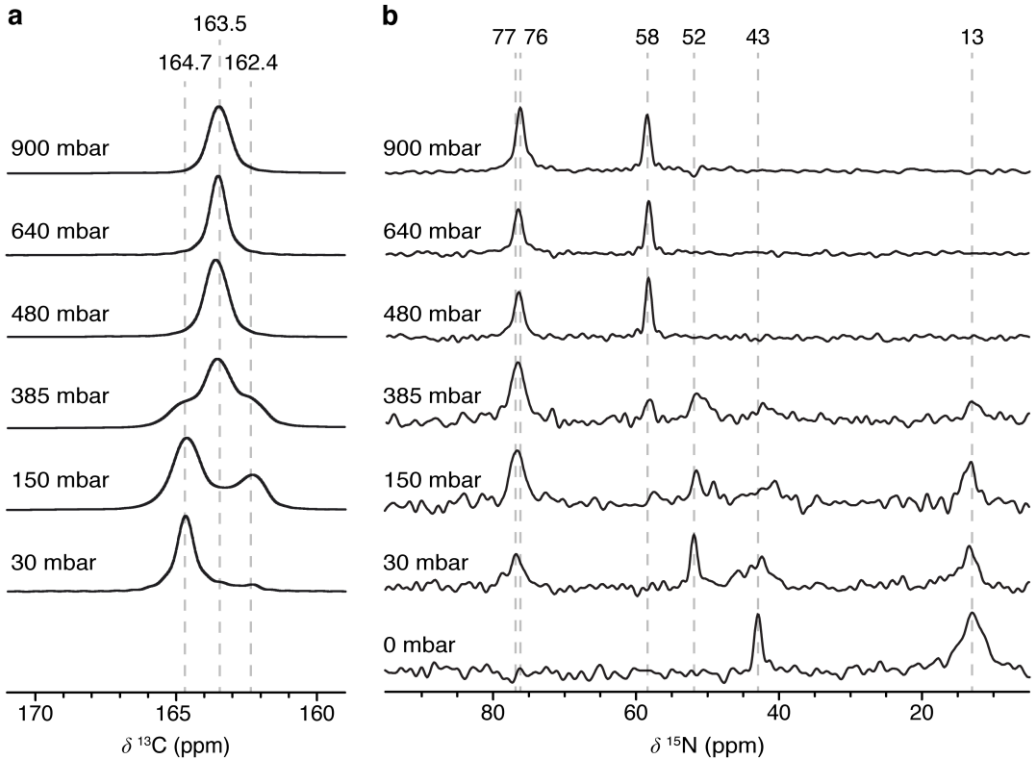


**Figure 4.** (a) $^{13}$C MAS (15 kHz) NMR (16.4 T) spectra of dmen–$Mg_2$(dobpdc) dosed at 24 °C and various pressures of $^{13}CO_2$. Spectra were acquired by direct excitation with continuous wave $^1$H decoupling and a recycle delay time of 128 s, which was sufficiently long to yield quantitative intensities. Deconvolution of the 150 and 385 mbar spectra yielded relative integrations of 0.35:0.41:0.24 and 0.16:0.56:0.28, respectively, for the resonances at 164.7, 163.5, and 162.4 ppm, respectively. (b) $^{15}$N MAS (10 kHz) NMR (16.4 T) spectra of dmen–$Mg_2$(dobpdc) at various pressures of $^{13}CO_2$ acquired by cross-polarization with a contact time of 2 ms.

and 40 °C, the quantity of $CO_2$ adsorbed in the material dropped sharply to ~1.0 $CO_2$ per diamine within the first 3 min before decreasing more gradually over the remaining measurement period. This behavior indicates that $CO_2$ uptake to 1.0 $CO_2$ per diamine in dmen–$Mg_2$(dobpdc) is due to chemisorption, whereas subsequent uptake is a result of physisorption.

We next measured $CO_2$ desorption isobars using a ramp rate of 1 °C/min, starting from the equilibrated states at various temperatures (Figure 3c). For states prepared at temperatures above 40 °C, loss of $CO_2$ from the material occurred gradually until stepped desorption at 0.5 $CO_2$ per dmen. For equilibrated states prepared at 30 and 40 °C, $CO_2$ loss occurred gradually until 1.0 $CO_2$ per diamine when clear double-step desorption occurred, with each step corresponding to a loss of approximately 0.5 $CO_2$ per diamine. DSC data collected under conditions designed to mimic the 30 °C desorption isobar feature two clear sharp endothermic peaks corresponding to the two desorption steps, indicating that these steps result from cooperative desorption of $CO_2$ (Figure S7). Overall, the TGA experiments suggest that it is possible to achieve a loading of 1.0 $CO_2$ per diamine in dmen–$Mg_2$(dobpdc) under pure $CO_2$ at 30 °C, in contrast to all previous reports. However, this full-capacity state is not accessible using typical adsorption measurements, due to the apparently slow kinetics involved in transitioning from half capacity (0.5 $CO_2$ per diamine) to full capacity (1.0 $CO_2$ per diamine). This is a phenomenon that has not been encountered with other diamine-appended materials exhibiting two-step adsorption, such as *n*Pr-2–$Mg_2$(dobpdc),[14,16] suggesting that the mechanism of $CO_2$ uptake in dmen–$Mg_2$(dobpdc) is unique. Notably, $CO_2$ isobars obtained for dmen–$Mg_2$(dobpdc) in the presence of water vapor suggest that humidity does not substantially change the adsorption behavior of this material (see Figure S38).

As further support for our hypothesis, we dosed a sample of dmen–$Mg_2$(dobpdc) directly with 1 bar of $CO_2$ at temperatures ranging from 30 to 75 °C and then collected desorption data (Figure 3d), hereafter referred to as shock–desorption isotherms. This protocol should enable the material to avoid the half-capacity trap encountered upon gradual adsorption of $CO_2$ from the activated state. Consistent with the TGA data, the 1-bar capacities determined from shock–desorption isotherms collected at 30 and 40 °C are 1.3 and 1.0 $CO_2$ per diamine, respectively, significantly higher than the capacities determined under the same conditions from standard adsorption isotherm measurements.

**NMR Spectra.** Solid-state magic-angle spinning (MAS) $^{13}$C and $^{15}$N NMR data were collected to elucidate the species formed upon $CO_2$ adsorption in dmen–$Mg_2$(dobpdc) over a range of pressures as high as 1 bar. Each NMR sample was prepared by dosing the activated material with $^{13}CO_2$ such that the target pressure would be achieved after a 48-h equilibration period (see the Experimental Section for details). The $^{13}$C spectrum collected at 24 °C under 1 bar of $^{13}CO_2$ features two resonances at 163.5 and 124.8 ppm, which are assigned to chemisorbed and physisorbed $CO_2$, respectively (Figure S21).[24] The single chemical shift for chemisorbed $CO_2$ suggests formation of a single carbamate environment and is similar to chemical shifts reported previously for ammonium carbamate chains formed in diamine–$Mg_2$(dobpdc).[24] Quantitative integration of both peaks yielded a chemisorbed:physisorbed ratio of 1.00:0.29, consistent with the TGA results (Figure S10).

The $^{13}$C NMR spectra of dmen–$Mg_2$(dobpdc) obtained under $^{13}CO_2$ pressures of 480, 640, and 900 mbar also feature a single resonance for chemisorbed $CO_2$ at 163.6, 163.5, and 163.5 ppm,

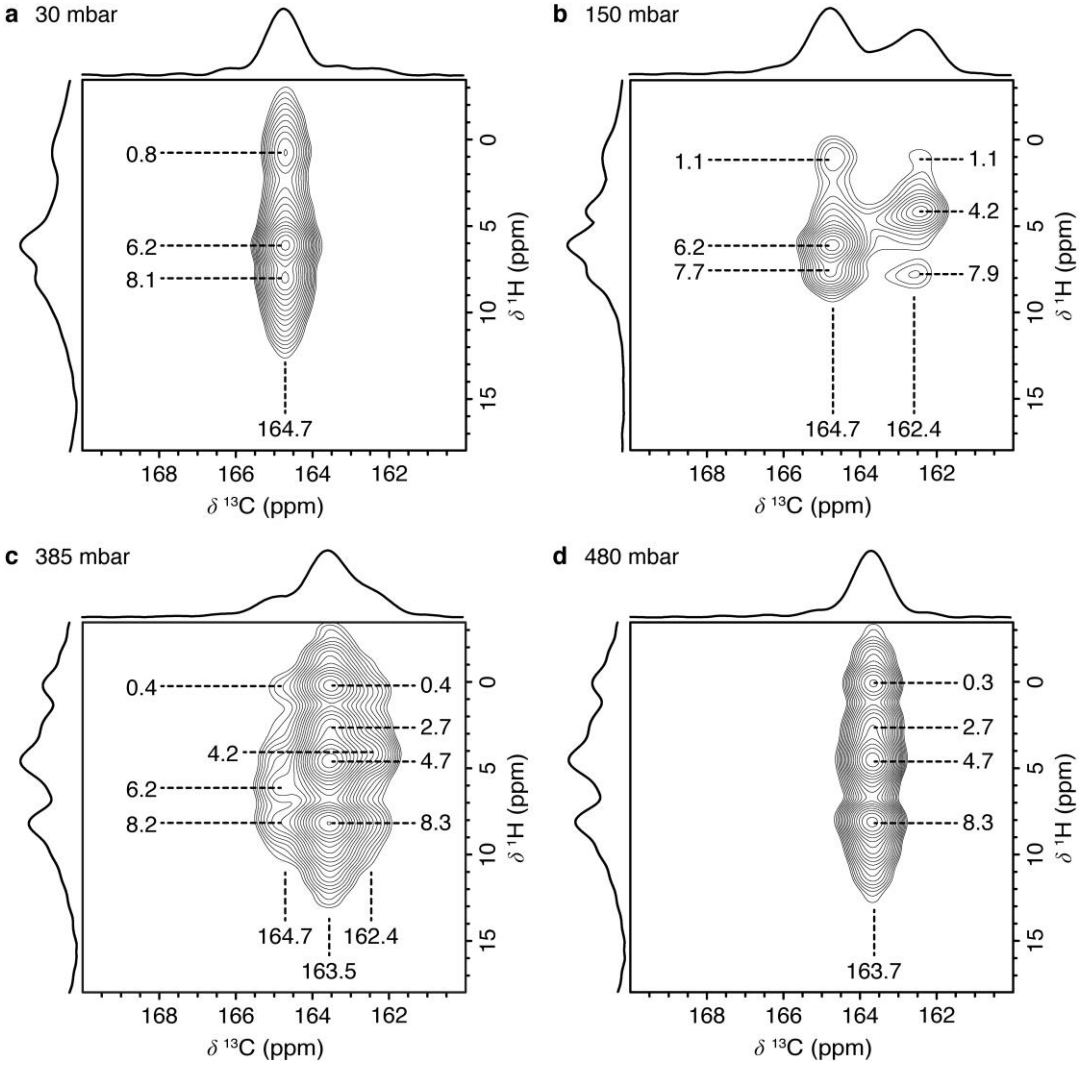


**Figure 5**. $^{1}H$–$^{13}C$ MAS (15 kHz) NMR (16.4 T) HETCOR spectra of dmen–$Mg_2$(dobpdc) dosed with $^{13}CO_2$ to achieve pressures of (a) 30 mbar, (b) 150 mbar, (c) 385 mbar, and (d) 480 mbar at 24 °C. The contact time for cross-polarization was 100 μs to probe $^{1}H$ nuclei close to the carbamate carbon.

respectively, consistent with the 1.0-bar data (Figure 4a). However, in the spectrum obtained under 385 mbar of $^{13}CO_2$, two additional $^{13}C$ resonances for chemisorbed $CO_2$ are present at 162.4 and 164.7 ppm. Notably, the relative intensities of these three chemisorbed peaks are different at lower pressures approaching that associated with the half-capacity state (see Figure 3d). In particular, for a sample dosed with 150 ppm of $^{13}CO_2$, the resonances at 164.7 and 162.4 ppm dominate, while at 30 ppm of $CO_2$, the species at 164.7 ppm represents the major chemisorbed product. The $^{15}N$ NMR spectrum of the activated framework (Figure 4b) features two resonances at 13 and 43 ppm, corresponding to the two ends of the appended diamine. Dosing with 30 mbar of $^{13}CO_2$ resulted in the appearance of two new resonances at 52 and 77 ppm, assigned to carbamate and ammonium groups from a single ammonium carbamate chain conformation.[17,24] The $^{15}N$ spectra obtained under intermediate $^{13}CO_2$ pressures of 150 and 385 mbar feature a mixture of resonances, indicative of multiple ammonium carbamate environments, while above 480 mbar of $^{13}CO_2$, a single species is again present with peaks at 58 and 76 ppm. Overall, the $^{13}C$ and $^{15}N$ NMR data indicate that a single ammonium carbamate species exists at low $CO_2$ pressures that is distinct from the species arising at high pressures.

Two-dimensional HETCOR data were collected for samples dosed with 30, 150, 385, and 480 mbar of $^{13}CO_2$ (Figure 5) to gain insight into the nature of these two species. The HETCOR spectra obtained at intermediate pressures of 150 and 384 mbar feature a mixture of different correlation groups, while the spectra at 30 and 480 mbar each have one major correlation group, at 164.7 and 163.7 ppm, respectively. Additional HETCOR data collected for samples dosed with $^{13}CO_2$ at 640 and 900 mbar feature correlations consistent with the 480-mbar spectrum (Figure S27). The observed correlations at all pressures are consistent with formation of ammonium carbamate chains, which are characterized by $^{1}H$ resonances for the diamine backbone (<4 ppm), a strong resonance for the carbamate hydrogen (between 4 and 6.5 ppm), and a weaker resonance for the ammonium hydrogens (>6.5 ppm).[24]

It is important to note here that ammonium carbamate chain formation in diamine–$Mg_2$(dobpdc) can occur in two different directions. As a result of the linker inversion symmetry, in the parent framework, adjacent $Mg^{2+}$ helices feature bound carboxylate and phenoxide groups oriented in opposite directions (Figure 6a).[26] We define a direction for each helix based on a vector pointing from the carboxylate to phenoxide group on each

linker, hereafter referred to as the carboxylate–phenoxide direction. As such, we can also define an inherent direction for the ammonium carbamate chains that form upon $CO_2$ uptake, based on the orientation of the carbamate group relative to the carboxylate–phenoxide direction (Figure 6b). In particular, we refer to the scenario where the carbamate groups point along the carboxylate–phenoxide direction as ammonium carbamate chains in the *forward* direction, whereas when the $NCOO^-$ groups point against the carboxylate–phenoxide direction, we refer to this scenario as the *reverse* direction. We surveyed published single-crystal X-ray diffraction data for a number of diamine–$Zn_2$(dobpdc) materials and found that, upon $CO_2$ uptake, the vast majority form ammonium carbamate chains in the forward direction.[13,15,26] Interestingly, the only exception is dmen–$Zn_2$(dobpdc), which adsorbs $CO_2$ to form ammonium carbamate chains in the reverse direction with an occupancy of 44%, with the remaining metal sites occupied by unreacted diamine.[15] We considered that the different ammonium carbamate structures that form in dmen–$Mg_2$(dobpdc) at low and high $CO_2$ pressures, as characterized by solid-state NMR spectroscopy, might correspond to ammonium carbamates running in the reverse and forward directions, respectively, and therefore that a switch in chain direction is required to achieve $CO_2$ uptake to full capacity.

**Computational Modeling.** To investigate this possibility, we used vdW-DFT to calculate geometry-optimized structures for the activated framework as well as the half- and full-capacity structures with chains running in both the forward and reverse directions (Figure 7a–e). We also calculated a full-capacity mixed structure (Figure 7f), consisting of neighboring forward and reverse direction chains, as a potential configuration at intermediate pressures. Calculated $CO_2$ binding energies and NMR chemical shifts determined for these structures are given in Table 1, along with the experimental chemical shifts. Interestingly, the calculations revealed that at half capacity, $CO_2$ binding is stronger in the reverse structure, whereas at full capacity $CO_2$ binding is stronger in the forward structure. At half capacity, the $CO_2$ binding energy in the reverse direction is −105.0 kJ/mol, substantially larger than the value of −66.2 kJ/mol calculated for the half-capacity forward direction. The predicted added stabilization for the reverse structure at half capacity may be due in part to favorable hydrogen bonding interactions between the unreacted diamines and the ammonium groups in the adjacent chains (Figure 7c). The calculated binding energy in the reverse direction is also consistent with the adsorption enthalpy calculated from the $CO_2$ adsorption isotherms (−93±7 kJ/mol) and the desorption enthalpy calculated from the $CO_2$ shock–desorption isotherms (95±5 kJ/mol) at a loading of 0.25 $CO_2$ per diamine, used to capture the half-capacity step region (Figures S16 and S18). The discrepancy of ~10 kJ/mol between the vdW-DFT binding energy and the experimental adsorption enthalpy is typical for diamine–$Mg_2$(dobpdc) systems.[28]

Additionally, our experimental $CO_2$ adsorption enthalpy is in reasonable agreement with the adsorption enthalpy of −82 kJ/mol previously determined for dmen–$Mg_2$(dobpdc) at a loading of 0.25 $CO_2$ per diamine.[17] In the full capacity structures, $CO_2$ binding in the forward structure is more favorable than in the reverse and mixed structures (−71.2 kJ/mol versus −60.3 and −65.2 kJ/mol, respectively). Because only one ammonium carbamate resonance was characterized in the $^{15}N$ NMR spectra at high $^{13}CO_2$ pressures (Figure 4), we can rule out the possibility of a mixed structure at full capacity. We note that a previous study used vdW-DFT to evaluate $CO_2$ adsorption in dmen–$Mg_2$(dobpdc) assuming the full-capacity reverse structure and reported a binding energy of −83.9 kJ/mol.[29] However, that report used a different vdW-DFT functional (PBE[30] + D3[31]) than employed here (rPBE[32] + D3), and a comparison of the two functionals using the reference material m-2-m–$Zn_2$(dobpdc) (m-2-m = *N,N'*-dimethylethylenediamine) revealed that our choice of functional may yield more accurate $CO_2$ binding energies (see Table S4).

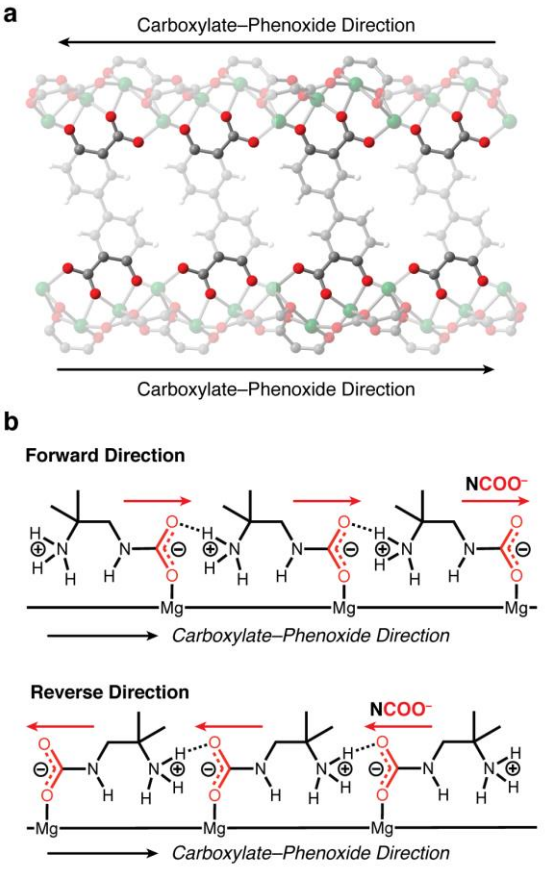


**Figure 6.** (a) Illustration of the carboxylate–phenoxide direction in $Mg_2$(dobpdc). Green, red, gray, and white spheres represent Mg, O, C, and H atoms, respectively. (b) Depiction of ammonium carbamate chain formation in dmen–$Mg_2$(dobpdc) occurring in the forward direction ($NCOO^-$ points along the carboxylate-phenoxide direction) and reverse direction ($NCOO^-$ points against the carboxylate-phenoxide direction).

Based on these results, we assigned the resonances in the spectra collected under 480, 640, and 900 mbar of $^{13}CO_2$ to the forward direction structure, and the resonances under 30 mbar of $^{13}CO_2$ to the reverse direction structure. The distinct chemical shifts may arise due to hydrogen bonding interactions between the ammonium group and the linker in the forward direction structure, and the carbamate group and the linker in the reverse direction structure (Figure 7). We quantified the goodness of fit for each proposed structure using the parameter $\chi_v^2 = \frac{1}{n}\sum_{i=1}^{n}\left(\frac{\delta_i^{exp} - \delta_i^{calc}}{RMSD_i}\right)^2$, where $\delta_i^{exp}$ and $\delta_i^{calc}$ are the experimental

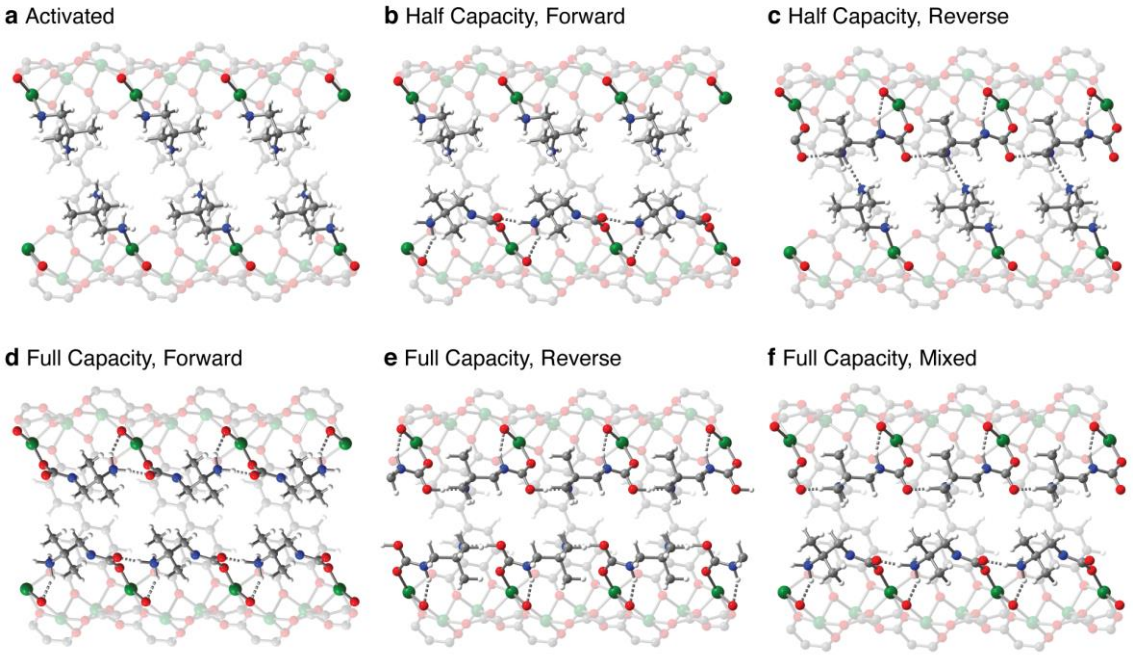


**Figure 7**. Geometry-optimized vdW-DFT structures of $CO_2$ adsorbed in dmen–$Mg_2$(dobpdc). Green, red, blue, gray, and white spheres represent Mg, O, N, C, and H atoms, respectively. Hydrogen bonds are shown as dashed lines.

**Table 1. Experimental and Calculated NMR Chemical Shifts and Calculated $CO_2$ Adsorption Energies**

| Structure | $\Delta E_{ads}$ (kJ/mol) | δ $^{13}$C (ppm) | δ $^{15}$N (ppm) | δ $^{1}$H (ppm) [a] |
|---|---|---|---|---|
| Activated | — | — | Metal-Bound Amine: 7.3<br>Free Amine: 35.7 | — |
| HC (30 mbar $^{13}CO_2$) | — | Carbamate: 164.7 | Ammonium: 52<br>Carbamate: 76<br>Metal-Bound Amine: 13<br>Free Amine: 43 | Ammonium: 8.1<br>Carbamate: 6.2 |
| Calc. HC Reverse | −105.0 | Carbamate: 164.7 | Ammonium: 50.6<br>Carbamate: 83.3<br>Metal-Bound Amine: 7.3<br>Free Amine: 32.6 | Ammonium: 8.2<br>Carbamate: 6.8 |
| Calc. HC Forward | −66.2 | Carbamate: 162.7 | Ammonium: 58.7<br>Carbamate: 78.3<br>Metal-Bound Amine: 6.7<br>Free Amine: 39.1 | Ammonium: 8.3<br>Carbamate: 4.8 |
| FC (900 mbar $^{13}CO_2$) | — | Carbamate: 163.5 | Ammonium: 58<br>Carbamate: 77 | Ammonium: 8.3<br>Carbamate: 4.7 |
| Calc. FC Forward | −71.2 | Carbamate: 162.3 | Ammonium: 57.3<br>Carbamate: 77.4 | Ammonium: 8.3<br>Carbamate: 4.6 |
| Calc. FC Reverse | −60.3 | Carbamate: 164.9 | Ammonium: 55.0<br>Carbamate: 83.7 | Ammonium: 7.7<br>Carbamate: 8.3 |
| Calc. FC Mixed | −65.2 | Carbamate forward: 162.9<br>Carbamate reverse: 165.3 | Ammonium forward: 57.1<br>Carbamate forward: 78.7<br>Ammonium reverse: 55.6<br>Carbamate reverse: 84.1 | Ammonium forward: 8.2<br>Carbamate forward: 4.8<br>Ammonium reverse: 7.6<br>Carbamate reverse: 8.2 |

[a] The ammonium group is assumed to rotate on the NMR timescale, and the reported shift is an average for the three H atoms. HC = half capacity and FC = full capacity.

and calculated chemical shifts, *i* indexes the ammonium hydrogen, carbamate hydrogen, carbamate carbon, ammonium nitro-

gen, and carbamate nitrogen, and $RMSD_i$ are the previously reported root mean squared deviations between experimental and calculated chemical shifts for the respective groups.[24] A value of $\chi_\nu^2 << 1$ is indicative of a good fit, whereas $\chi_\nu^2 >> 1$ is indicative of a poor fit relative to the expected deviation. At half capacity, the $\chi_\nu^2$ value is 0.64 for the forward direction and 0.25 for the reverse direction, whereas at full capacity, the $\chi_\nu^2$ value is 0.07 for the forward direction and 2.00 for the reverse direction. These values support the structural assignments at half and full capacity and the transition from a reverse to a forward direction ammonium carbamate chain as the material adsorbs $CO_2$ to full capacity. At intermediate $^{13}CO_2$ pressures, the NMR spectra feature resonances for the forward and reverse direction chains (163.5 and 164.7 ppm, respectively), as well as a third ammonium carbamate $^{13}C$ resonance at 162.4 ppm, with a carbamate hydrogen correlation at 4.2 ppm. The correlation suggests this species also corresponds to chains in the forward direction. The slight difference between the two forward-direction $^{13}C$ carbamate shifts could arise due to the presence of differing electronics at neighboring sites, which may feature unreacted diamine or forward direction chains (Table 1).

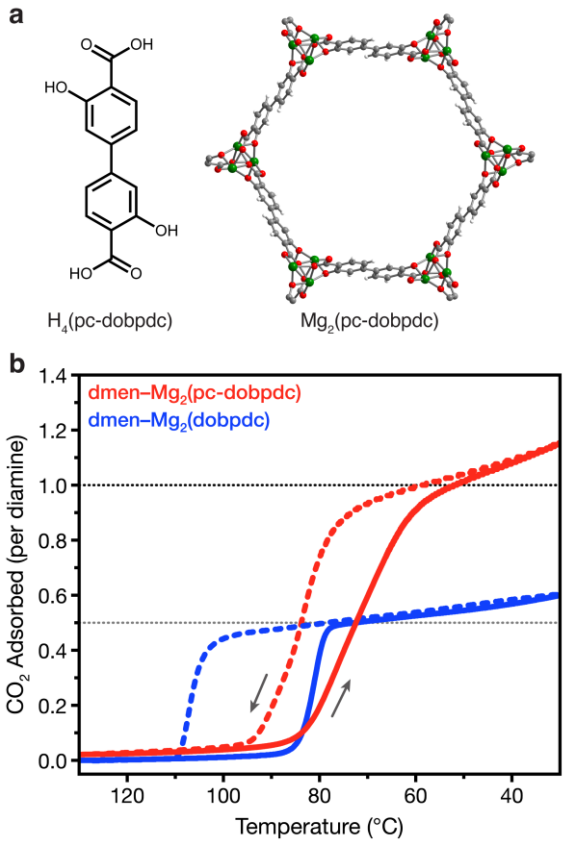


**Figure 8.** (a) Structures of the $H_4$(pc-dobpdc) linker and a single pore of $Mg_2$(pc-dobpdc). Green, blue, gray, and white spheres represent Mg, O, C, and H atoms, respectively. (b) Isobars obtained for dmen–$Mg_2$(pc-dobpdc) and dmen–$Mg_2$(dobpdc) under pure $CO_2$. Adsorption and desorption data are shown as solid and dashed lines, respectively. Gray and black dashed lines indicate capacities of 0.5 $CO_2$ per diamine (half capacity) and 1 $CO_2$ per diamine (full capacity), respectively, and gray arrows indicate the direction of temperature change. For dmen–$Mg_2$(dobpdc) and dmen–$Mg_2$(pc-dobpdc), 1 $CO_2$ per diamine is 4.0 mmol/g, or 17.8 g/100g.

The proposed switching of the chain direction at different pressures ultimately explains the unusual adsorption kinetics observed for dmen–$Mg_2$(dobpdc). The transition from the activated state to either the half-capacity or full-capacity state is rapid, because the only activation barrier is that associated with the formation of a single ammonium carbamate chain. However, transitioning from the half- to full-capacity state requires that all of the adsorbed ammonium carbamate chains switch direction to the equilibrium configuration, a transition that is likely associated with a large activation barrier.

**Achieving Full Capacity with dmen–$Mg_2$(pc-dobpdc).** The calculated structures for the full-capacity configurations (Figure 7d and e) provide some insight into a possible origin of the ammonium carbamate chain direction switching. In particular, the *gem*-dimethyl groups on the diamine backbone are oriented toward neighboring diamines in the reverse structure, whereas they are oriented away from neighboring diamines in the forward structure (Figure 7d and e), and thus steric interactions may in part influence the kinetics of $CO_2$ uptake in dmen–$Mg_2$(dobpdc). We have previously shown that unfavorable steric interactions in diamine–$Mg_2$(dobpdc) and associated double-step $CO_2$ uptake behavior can be avoided by using the isomeric framework $Mg_2$(pc-dobpdc) (pc-dobpdc = 3,3′-dioxidobiphenyl-4,4′-dicarboxylate), which features a more symmetric hexagonal pore structure and a slightly longer distance between nearest neighbor diamines in the *ab* plane (Figure 8a).[16] Importantly, diamine–$Mg_2$(pc-dobpdc) exhibits a single $CO_2$ adsorption step at a pressure that is approximately the same as the lower pressure step for the corresponding diamine–$Mg_2$(dobpdc). We hypothesized that by removing any steric effects encountered using $Mg_2$(dobpdc) while retaining the appended dmen, it might be possible to access a material exhibiting uninhibited $CO_2$ adsorption to full capacity, in the optimal pressure region for coal flue gas capture.[16,17]

Gratifyingly, we found that dmen–$Mg_2$(pc-dobpdc) indeed exhibits single-step adsorption of $CO_2$ to full capacity, with an adsorption step at approximately the same temperature as in dmen–$Mg_2$(dobpdc) (Figure 8b), suggesting that interactions between neighboring diamines in the *ab* plane are the cause of the unusual $CO_2$ adsorption properties of dmen–$Mg_2$(dobpdc). Additional isobar experiments revealed that dmen–$Mg_2$(pc-dobpdc) retains its step-shaped adsorption profile under various partial pressures of $CO_2$ and humid conditions (Figures S48 and S49). Furthermore, $CO_2$ uptake in the material under humid conditions is essentially unchanged following exposure to wet $CO_2$ for 12 h at 140 °C (Figure S50). Overall, these results indicate that dmen–$Mg_2$(pc-dobpdc) is an exceptionally promising adsorbent for carbon capture from coal flue gas under industrially relevant conditions.

## CONCLUSIONS

The foregoing results revealed that the unusual $CO_2$ adsorption properties of dmen–$Mg_2$(dobpdc) arise due to the presence of a metastable state at half capacity that very slowly converts to the full-capacity structure corresponding to 1 $CO_2$ per diamine. Using non-traditional $CO_2$ dosing methods involving isothermal waiting periods and shock–desorption, it is possible to bypass the metastable trap at half-capacity and achieve saturation of dmen–$Mg_2$(dobpdc). We propose that it may be beneficial for these alternative techniques to be adopted as part of the standard characterization regimen for new metal–organic frameworks, particularly those exhibiting non-traditional guest uptake, to verify that capacities determined using standard isobar and isotherm measurements accurately reflect equilibrated capacities.

Solid-state MAS NMR spectroscopy coupled with vdW-DFT calculations indicate that the barrier to $CO_2$ saturation in dmen–$Mg_2$(dobpdc) arises due to differing orientations of the ammonium carbamate chains in the half- and full-capacity structures. In particular, at low loadings when the half-capacity configuration is favored, alternating diamines react with $CO_2$ to form ammonium carbamate chains along a direction that is opposite the carboxylate–phenoxide vector defined for a given metal helix. In contrast, the full-capacity configuration is accessed at high loadings and features ammonium carbamate chains oriented along the carboxylate–phenoxide vector. At intermediate $CO_2$ loadings, both reverse and forward direction chains are present. These results mark the first reported instance of ammonium carbamate chains formed in diamine-functionalized MOFs altering their orientation as a function of $CO_2$ loading. By alleviating steric interactions between diamines in dmen–$Mg_2$(pc-dobpdc), it is possible to access the full material capacity in a single adsorption step, at a temperature suitable for $CO_2$ capture from the flue gas of coal-fired power plants.

## EXPERIMENTAL DETAILS

**General Procedures.** Reagents and solvents were purchased from commercial suppliers at reagent grade purity or higher and used without further purification. The linker $H_4$(dobpdc) was purchased from Hangzhou Trylead Chemical Technology Co. Ultrahigh purity (99.999%) He and $N_2$ and research grade (99.998%) $CO_2$ were used for all adsorption experiments. Isotopically labeled $^{13}CO_2$ used in solid-state NMR experiments was purchased from Sigma-Aldrich (99 atom% $^{13}C$, < 3 atom% $^{18}O$). Solution-state $^1H$ NMR spectra were collected on a Bruker AMX 300 MHz NMR spectrometer and referenced to residual dimethyl sulfoxide (2.50 ppm) or chloroform (7.26 ppm). The ligand $H_4$(pc-dobpdc) and framework $Mg_2$(pc-dobpdc) were prepared following previously reported procedures.[16]

**Synthesis of $Mg_2$(dobpdc)**. The framework $Mg_2$(dobpdc) was synthesized following a literature procedure, which is reproduced here with details relevant to this work.[13] The ligand $H_4$(dobpdc) (4.95 g, 18.1 mmol) and $Mg(NO_3)_2{\cdot}6H_2O$ (5.77g, 22.5 mmol) were dissolved in 100 mL of a 55:45 (v:v) methanol:*N*,*N*-dimethylformamide (DMF) mixture using sonication. The solution was filtered to remove any undissolved particulates and added to a 250 mL glass pressure vessel with a stir bar. The reactor was sealed with a Teflon cap and heated in a silicone oil bath at 120 °C for 20 h. The crude white powder was isolated by filtration and soaked three times in 200 mL of DMF for a minimum of 3 h per soak at 60 °C, followed by solvent exchange by soaking three times in 200 mL of methanol for a minimum of 3 h per soak at 60 °C. The framework was stored in methanol when not in use. The methanol-solvated framework was collected by filtration and heated under flowing $N_2$ for 12 h at 180 °C to yield fully desolvated $Mg_2$(dobpdc) as a white powder.

**Synthesis of Diamine-Functionalized Metal–Organic Frameworks**. Diamine-appended MOFs were synthesized following the literature procedures for similar diamine–$Mg_2$(dobpdc)[13] and diamine–$Mg_2$(pc-dobpdc)[16] materials. Methanol-solvated materials ($Mg_2$(dobpdc), $Mg_2$(pc-dobpdc)) were filtered and washed five times with 10 mL toluene. The filtered framework (~20 mg) was then added to 5 mL of a 20% (v:v) solution of diamine in toluene. After soaking for 24 h, the solid was obtained by filtration and washed five times with 10 mL of toluene to remove excess diamine before proceeding to activation. Diamine loadings were determined by obtaining quantitative $^1H$ NMR (300 MHz, DMSO-$d_6$) spectra of the digested frameworks. All diamine loadings were between 120% and 200% before activation, and 100 ± 5% after activation (sample-specific activation temperatures specified below). For digestion, ~5 mg of material was dissolved in a solution containing 750 μL of dimethyl sulfoxide-$d_6$ and 50 μL of deuterium chloride solution (35 g/100g in $D_2O$, ≥ 99 atom% D).

**Thermogravimetric Analysis**. Dry thermogravimetric analysis experiments were conducted using a TA Instruments TGA Q5000, and humid TGA experiments were conducted using a TA Instruments TGA Q50. Dry and humid isobar measurements were conducted following previously reported methods.[16] Samples were measured at ambient pressures using a gas flow rate of 25 mL/min. For humid TGA experiments, the incident gas stream was passed through two room-temperature water bubblers before entering the furnace. As-synthesized samples of e-2–$Mg_2$(dobpdc), *n*Pr-2–$Mg_2$(dobpdc), and dmen–$Mg_2$(dobpdc) were activated at 130 °C under flowing $N_2$ for 30 min, and dmen–$Mg_2$(pc-dobpdc) was activated at 140 °C under flowing $N_2$ for 30 min prior to TGA measurements, at which point the masses of all samples had stabilized. Masses are uncorrected for buoyancy effects. Custom $CO_2/N_2$ blends of 15% and 5% were purchased from Praxair.

**Differential Scanning Calorimetry**. Differential scanning calorimetry experiments were conducted using a TA Instruments Q200 DSC. DSC samples were analyzed under ambient pressure using a gas flow rate of 25 mL/min. Samples were activated at 130 °C under flowing $N_2$ for 30 min via TGA to determine the activated sample mass, at which point the masses of all samples had stabilized. The samples were then transferred from the TGA to DSC and reactivated at 130 °C under flowing He for 30 min prior to DSC measurements. The lid on the DSC pan is slightly ajar to allow for gas flow, contributing to potential heat loss and error.

**Gas Adsorption Isotherms**. Isotherms for $CO_2$ adsorption were collected on a Micromeretics 3Flex gas adsorption analyzer using previously detailed procedures.[24] Shock–desorption isotherms were collected using the same experimental setup as used for collecting desorption isotherms. However, in contrast to the protocol for a standard desorption isotherm, wherein the first data point is taken directly after collecting an adsorption isotherm, in a shock–desorption isotherm the first data point is obtained after first directly dosing the evacuated sample with 1 bar of $CO_2$. Approximately 100 mg of diamine-functionalized MOF was added to the sample tube for adsorption analysis. To account for fluctuations in temperature of the heating bath at different times, $CO_2$ adsorption isotherms and shock–desorption isotherms were performed on two different aliquots of material using the same temperature bath at the same time. Samples were activated at 120 °C for 3 h *in vacuo* between measurements. Adsorption isotherms and shock–desorption isotherms used an equilibration interval of 30 s, where the sample is considered equilibrated when the pressure change per equilibration time interval is less than 0.01% of the average pressure in the time interval over 11 consecutive equilibration time intervals. Isosteric enthalpies and entropies of adsorption were calculated following reported procedures employing Clausius–Clapeyron relation.[13–15] Langmuir surface areas were obtained from a $N_2$ isotherm at 77 K using a liquid $N_2$ bath. Langmuir surface areas of $Mg_2$(dobpdc) and $Mg_2$(pc-dobpdc) determined from the 77 K $N_2$ isotherm were 4020 and 3470 $m^2/g$, respectively.

**Sample Preparation for Solid-State NMR Spectroscopy**. Sample preparation for solid-state MAS NMR analysis closely followed the literature procedure, reproduced here with minor changes.[24] Activated diamine-appended framework samples were packed into 3.2 mm rotors inside a nitrogen-filled glovebag and subsequently evacuated inside a home-built gas-dosing manifold for 30 min. Samples were dosed with $^{13}CO_2$ gas at room temperature (24 °C) and allowed to equilibrate for at least 48 h. Gas pressures were recorded immediately before closing the rotor inside the gas manifold at the end of the 48 h. For NMR spectra of wet samples, the sample was first dosed with $^{13}CO_2$ in the same manner as the dry experiments. The rotor was then removed from the gas manifold, uncapped, exposed to a $CO_2$ stream that passed through a water bubbler at 24 °C. After 1 h of exposure to the wet $CO_2$ stream, the rotor was closed again. For the $CO_2$ stream, we used 100% $CO_2$ for the 1.0 bar of $^{13}CO_2$ sample, and we used 15% $CO_2$ (balance $N_2$) for the 150 mbar of $^{13}CO_2$ sample.

**Solid-State NMR Experiments**. All solid-state NMR experiments were performed using a 16.4 T magnet. All $^1H$ and $^{13}C$ experiments were conducted with spinning at 15 kHz, and all $^{15}N$ experiments were conducted with spinning at 10 kHz. The $^1H$ NMR spectra were acquired with direct excitation and a delay time of 4 s, which was sufficiently long to yield quantitative results. Quantitative $^{13}C$ NMR spectra were acquired by direct excitation, continuous wave $^1H$ decoupling, and a delay time of 128 s, which was sufficiently long to yield quantitative results. Dmfit software was used to deconvolute the NMR peaks and quantify integrations.[33] All other $^{13}C$ NMR experiments, in addition to

all $^{15}$N experiments, were acquired by cross-polarization from $^{1}$H. All cross-polarization experiments used continuous wave $^{1}$H decoupling at ~80 kHz radio-frequency field strength and with contact times of 1 ms for $^{13}$C and 2 ms for $^{15}$N. For 2D $^{1}$H–$^{13}$C experiments, we used a HETCOR sequence 90°($^{1}$H) – $t_1$ – cross-polarization – $t_2$, again using cross-polarization from $^{1}$H and continuous wave $^{1}$H decoupling. $^{1}$H, $^{13}$C, and $^{15}$N NMR shifts were referenced respectively to 1.8 (adamantane), 38.5 (adamantane, tertiary carbon—left resonance), and 33.4 ppm (glycine)[34]. NMR experiments were performed at 24 °C without temperature control.

**Computational Details**. We performed first-principles density functional theory calculations within the generalized gradient approximation (GGA) of revised Perdew-Burk-Ernzerhof (rPBE) with Pade approximation.[32] We used a plane-wave basis and projector augmented-wave (PAW)[35,36] psuedopotentials with the Vienna ab-initio Simulation Package (VASP) code.[37–40] To include the effect of the van der Waals dispersive interactions on binding energies, we performed structural relaxations with Grimme's D3 method (Becke-Jonson damping)[31] as implemented in VASP. For all calculations, we used (i) a 1 × 1 × 3 Monkhorst–Pack[41] *k*-point grid centered at the Γ-point of the Brillouin zone, (ii) a 900 eV plane-wave cutoff energy, and (iii) a $10^{-7}$ eV self-consistency criterion. We explicitly treated two valence electrons for Mg ($3s^2$), six for O ($2s^2 2p^4$), five for N ($2s^2 2p^3$), four for C ($2s^2 2p^2$), and one for H($1s^1$). All structural relaxations were performed with a Gaussian smearing of 0.05 eV.[42] The ions were relaxed until the Hellmann-Feynman forces are less than 0.01 eVÅ$^{-1}$.

To compute $CO_2$ binding energies, we optimized dmen–$Mg_2$(dobpdc) prior to $CO_2$ adsorption ($E_{\text{dmen–MOF}}$), interacting with $CO_2$ in the gas phase ($E_{CO2}$) within a 20 Å × 20 Å × 20 Å cubic supercell, and dmen–$Mg_2$ (dobpdc) with adsorbed $CO_2$ molecule ($E_{\text{CO2–dmen–MOF}}$) using vdW-corrected DFT. The binding energies ($E_B$) are obtained via the difference $E_B = E_{\text{CO}_2\text{–dmen–MOF}} - \left(E_{\text{dmen–MOF}} + E_{\text{CO}_2}\right)$. Starting structures for the activated and full-capacity reverse structures were obtained from single crystal X-ray structures of dmen–$Zn_2$(dobpdc).[15] The starting structure for the full-capacity forward structure was obtained from the calculated structure of a previous study.[24] Following these geometry optimizations, starting points for the half-capacity and mixed structures were obtained by overlaying the activated and full-capacity structures and relaxing symmetry constraints to the $P3_1$ space group.

For NMR simulations, we determined a $\sigma_{ref}$ value by comparing experimental $\delta_{iso}$ values to calculated $\sigma_{iso}$ values as the isotropic chemical shift ($\delta_{iso}$) is obtained from $\delta_{iso} = -(\sigma_{iso} - \sigma_{ref})$ where $\sigma_{ref}$ is a reference value. The $\sigma_{ref}$ values for $^{1}$H (31.2 ppm) and $^{13}$C (172.4 ppm) were obtained by first computing $\sigma_{iso}$ values for cocaine. The $\sigma_{ref}$ value for $^{15}$N (225.7 ppm) was determined by comparison of DFT-calculated $\sigma_{iso}$ and the experimental $\delta_{iso}$ value for glycine.[24] We compared the computed $\sigma_{iso}$ values for the cocaine molecule with the published experimental values,[43] with $\sigma_{ref}$ given as the y intercept of a linear fit with a fixed gradient of −1 in a plot of $\delta_{iso}$ (experimental) versus $\sigma_{iso}$ (calculated) (see Figure S30).

## ASSOCIATED CONTENT

### Supporting Information

The Supporting Information is available free of charge on the ACS Publications website.

Full characterization of adsorbents and additional experimental and computational details (PDF)

Structure files generated by vdW-DFT calculations with the rPBE functional and the D3 vdW correction (ZIP)

## AUTHOR INFORMATION


### Corresponding Authors

Jeffrey R. Long: jrlong@berkeley.edu
Jeffrey A. Reimer: reimer@berkeley.edu

### ORCID

Bhavish Dinakar: 0000-0002-7611-101X
Alexander C. Forse: 0000-0001-9592-9821
Henry Z.H. Jiang: 0000-0002-8086-3601
Jung-Hoon Lee: 0000-0002-2983-678X
Eugene J. Kim: 0000-0002-3474-3676
Surya T. Parker: 0000-0001-8534-8361
Rebecca L. Siegelman: 0000-0002-4249-6118
Phillip J. Milner: 0000-0002-4249-6118
Jeffrey R. Long: 0000-0002-5324-1321
Jeffrey A. Reimer: 0000-0002-4191-3725

### Present Addresses

[#] DuPont de Nemours, Inc. 200 Powder Mill Rd, Wilmington, DE, 19803, United States
[$] Department of Chemistry and Chemical Biology, Cornell University, Ithaca, New York 14853, United States


### Notes

The authors declare the following competing financial interest: J.R.L. has a financial interest in Mosaic Materials, Inc., a start-up company working to commercialize metal–organic frameworks for gas separations.

## ACKNOWLEDGMENT


This work was supported by the Department of Energy Office of Science, Office of Basic Energy Sciences under Award DE-SC0019992. We thank the NMR facility within the College of Chemistry for resources provided and Dr. Hasan Celik for his assistance with NMR experiments. Instruments within this NMR facility are supported in part by NIH S10OD024998. Solid-state NMR experiments were conducted using the 700 MHz magnet at the QB3 Berkeley NMR facility. Density functional theory calculations were conducted via the Molecular Graphics and Computation Facility (College of Chemistry, UC Berkeley) under NIH S10OD023532, and we thank Dr. Kathleen Durkin and Dr. Dave Small for assistance in running DFT calculations. Powder X-ray diffraction data were collected at Beamline 17-BM at the Advanced Photon Source, a DOE Office of Science User Facility, operated by Argonne National Laboratory under contract DE-AC02-06CH1135. We thank the Philomathia Foundation and Berkeley Energy and Climate Institute for a fellowship for A.C.F. We thank the National Institute of General Medical Sciences of the National Institutes of Health for a postdoctoral fellowship for P.J.M. (F32GM120799). The content is solely the responsibility of the authors and does not necessarily represent the official views of the National Institutes of Health. J.H.L.'s work was supported by the KIST Institutional Program (Project No. 2E30460). Computational resources provided by KISTI Supercomputing Centre (Project No. KSC-2019-CRE-0149) are gratefully acknowledged. We thank Dr. David Halat, Dr. Alicia Lund, Dr. Wei-Chih Liao, Dr. Haiyan Mao, Hao Zhuang, and Rohit Rungta for guidance on NMR experiments. We thank Dr. Jeffrey Martell, Matthew Dods, and Kaitlyn Engler for helpful discussions. We further thank Dr. Julia Oktawiec for assistance in preparing DFT structures, Maria Paley for assistance with powder X-ray diffraction measurements, and Dr. Katie Meihaus for editorial assistance.


## REFERENCES


(1) IPCC, 2018: Summary for Policymakers. In *Global Warming of 1.5°C.*; Masson-Delmotte, V., Zhai, P., Pörtner, H.-O., Roberts, D., Skea, J., Shukla, P. R., Pirani, A., Moufouma-Okia, W., Péan, C., Pidcock, R., Connors, S., Matthews, J. B. R., Chen, Y., Zhou, X., Gomis, M. I., Lonnoy, E., Maycock,

T., Tignor, M., Waterfield, T., Eds.; World Meteorological Organization: Geneva, Switzerland; pp 1–32.

(2) International Energy Agency. *Global Energy & $CO_2$ Status Report 2019*; Paris, France., 2019.

(3) Blanco, G.; Gerlach, R.; Suh, S.; Barrett, J.; de Coninck, H. C.; Diaz Morejon, C. F.; Mathur, R.; Nakicenovic, N.; Ofosu Ahenkora, A.; Pan, J.; Pathak, H.; Rice, J.; Richels, R.; Smith, S. J.; Stern, D. I.; Toth, F. L.; Zhou, P. Drivers, Trends and Mitigation. In *Climate Change 2014: Mitigation of Climate Change. Contribution of Working Group III to the Fifth Assessment Report of the Intergovernmental Panel on Climate Change*; Edenhofer, O., Pichs-Madruga, R., Sokona, Y., Farahani, E., Kadner, S., Seyboth, K., Adler, A., Baum, I., Brunner, S., Eickemeier, P., Kriemann, B., Savolainen, J., Schlömer, S., von Stechow, C., Zwickel, T., Minx, J. C., Eds.; Cambridge University Press: Cambridge, United Kingdom and New York, NY, USA, 2014.

(4) Pérez-Fortes, M.; Moya, J. A.; Vatopoulos, K.; Tzimas, E. $CO_2$ Capture and Utilization in Cement and Iron and Steel Industries. *Energy Procedia* **2014**, *63*, 6534–6543. https://doi.org/10.1016/j.egypro.2014.11.689.

(5) Barker, D. J.; Turner, S. A.; Napier-Moore, P. A.; Clark, M.; Davison, J. E. $CO_2$ Capture in the Cement Industry. *Energy Procedia* **2009**, *1* (1), 87–94. https://doi.org/10.1016/j.egypro.2009.01.014.

(6) Boot-Handford, M. E.; Abanades, J. C.; Anthony, E. J.; Blunt, M. J.; Brandani, S.; Dowell, N. M.; Fernández, J. R.; Ferrari, M.-C.; Gross, R.; Hallett, J. P.; Haszeldine, R. S.; Heptonstall, P.; Lyngfelt, A.; Makuch, Z.; Mangano, E.; Porter, R. T. J.; Pourkashanian, M.; Rochelle, G. T.; Shah, N.; Yao, J. G.; Fennell, P. S. Carbon Capture and Storage Update. *Energy Environ. Sci.* **2013**, *7* (1), 130–189. https://doi.org/10.1039/C3EE42350F.

(7) Rochelle, G. T. Amine Scrubbing for $CO_2$ Capture. *Science* **2009**, *325* (5948), 1652–1654. https://doi.org/10.1126/science.1176731.

(8) Wang, M.; Lawal, A.; Stephenson, P.; Sidders, J.; Ramshaw, C. Post-Combustion $CO_2$ Capture with Chemical Absorption: A State-of-the-Art Review. *Chem. Eng. Res. Des.* **2011**, *89* (9), 1609–1624. https://doi.org/10.1016/j.cherd.2010.11.005.

(9) Bourzac, K. We Have the Technology. *Nature* **2017**, *550* (7675), S66–S69. https://doi.org/10.1038/550S66a.

(10) Sumida, K.; Rogow, D. L.; Mason, J. A.; McDonald, T. M.; Bloch, E. D.; Herm, Z. R.; Bae, T.-H.; Long, J. R. Carbon Dioxide Capture in Metal–Organic Frameworks. *Chem. Rev.* **2012**, *112* (2), 724–781. https://doi.org/10.1021/cr2003272.

(11) McDonald, T. M.; Lee, W. R.; Mason, J. A.; Wiers, B. M.; Hong, C. S.; Long, J. R. Capture of Carbon Dioxide from Air and Flue Gas in the Alkylamine-Appended Metal–Organic Framework mmen-$Mg_2$(dobpdc). *J. Am. Chem. Soc.* **2012**, *134* (16), 7056–7065. https://doi.org/10.1021/ja300034j.

(12) McDonald, T. M.; Mason, J. A.; Kong, X.; Bloch, E. D.; Gygi, D.; Dani, A.; Crocellà, V.; Giordanino, F.; Odoh, S. O.; Drisdell, W. S.; Vlaisavljevich, B.; Dzubak, A. L.; Poloni, R.; Schnell, S. K.; Planas, N.; Lee, K.; Pascal, T.; Wan, L. F.; Prendergast, D.; Neaton, J. B.; Smit, B.; Kortright, J. B.; Gagliardi, L.; Bordiga, S.; Reimer, J. A.; Long, J. R. Cooperative Insertion of $CO_2$ in Diamine-Appended Metal-Organic Frameworks. *Nature* **2015**, *519* (7543), 303–308. https://doi.org/10.1038/nature14327.

(13) Siegelman, R. L.; McDonald, T. M.; Gonzalez, M. I.; Martell, J. D.; Milner, P. J.; Mason, J. A.; Berger, A. H.; Bhown, A. S.; Long, J. R. Controlling Cooperative $CO_2$ Adsorption in Diamine-Appended $Mg_2$(dobpdc) Metal–Organic Frameworks. *J. Am. Chem. Soc.* **2017**, *139* (30), 10526–10538. https://doi.org/10.1021/jacs.7b05858.

(14) Siegelman, R. L.; Milner, P. J.; Forse, A. C.; Lee, J.-H.; Colwell, K. A.; Neaton, J. B.; Reimer, J. A.; Weston, S. C.; Long, J. R. Water Enables Efficient $CO_2$ Capture from Natural Gas Flue Emissions in an Oxidation-Resistant Diamine-Appended Metal–Organic Framework. *J. Am. Chem. Soc.* **2019**, *141* (33), 13171–13186. https://doi.org/10.1021/jacs.9b05567.

(15) Milner, P. J.; Siegelman, R. L.; Forse, A. C.; Gonzalez, M. I.; Runčevski, T.; Martell, J. D.; Reimer, J. A.; Long, J. R. A Diaminopropane-Appended Metal–Organic Framework Enabling Efficient $CO_2$ Capture from Coal Flue Gas via a Mixed Adsorption Mechanism. *J. Am. Chem. Soc.* **2017**, *139* (38), 13541–13553. https://doi.org/10.1021/jacs.7b07612.

(16) Milner, P. J.; Martell, J. D.; Siegelman, R. L.; Gygi, D.; Weston, S. C.; Long, J. R. Overcoming Double-Step $CO_2$ Adsorption and Minimizing Water Co-Adsorption in Bulky Diamine-Appended Variants of $Mg_2$(dobpdc). *Chem. Sci.* **2017**, *9* (1), 160–174. https://doi.org/10.1039/C7SC04266C.

(17) Jo, H.; Lee, W. R.; Kim, N. W.; Jung, H.; Lim, K. S.; Kim, J. E.; Kang, D. W.; Lee, H.; Hiremath, V.; Seo, J. G.; Jin, H.; Moon, D.; Han, S. S.; Hong, C. S. Fine-Tuning of the Carbon Dioxide Capture Capability of Diamine-Grafted Metal–Organic Framework Adsorbents Through Amine Functionalization. *ChemSusChem* **2017**, *10* (3), 541–550. https://doi.org/10.1002/cssc.201601203.

(18) Lee, W. R.; Hwang, S. Y.; Ryu, D. W.; Lim, K. S.; Han, S. S.; Moon, D.; Choi, J.; Hong, C. S. Diamine-Functionalized Metal–Organic Framework: Exceptionally High $CO_2$ Capacities from Ambient Air and Flue Gas, Ultrafast $CO_2$ Uptake Rate, and Adsorption Mechanism. *Energy Environ. Sci.* **2014**, *7* (2), 744–751. https://doi.org/10.1039/C3EE42328J.

(19) Lee, W. R.; Jo, H.; Yang, L.-M.; Lee, H.; Ryu, D. W.; Lim, K. S.; Song, J. H.; Min, D. Y.; Han, S. S.; Seo, J. G.; Park, Y. K.; Moon, D.; Hong, C. S. Exceptional $CO_2$ Working Capacity in a Heterodiamine-Grafted Metal–Organic Framework. *Chem. Sci.* **2015**, *6* (7), 3697–3705. https://doi.org/10.1039/C5SC01191D.

(20) Drisdell, W. S.; Poloni, R.; McDonald, T. M.; Pascal, T. A.; Wan, L. F.; Pemmaraju, C. D.; Vlaisavljevich, B.; Odoh, S. O.; Neaton, J. B.; Long, J. R.; Prendergast, D.; Kortright, J. B. Probing the Mechanism of $CO_2$ Capture in Diamine-Appended Metal–Organic Frameworks Using Measured and Simulated X-Ray Spectroscopy. *Phys. Chem. Chem. Phys.* **2015**, *17* (33), 21448–21457. https://doi.org/10.1039/C5CP02951A.

(21) Kundu, J.; Stilck, J. F.; Lee, J.-H.; Neaton, J. B.; Prendergast, D.; Whitelam, S. Cooperative Gas Adsorption without a Phase Transition in Metal-Organic Frameworks. *Phys. Rev. Lett.* **2018**, *121* (1), 015701. https://doi.org/10.1103/PhysRevLett.121.015701.

(22) Kim, E. J.; Siegelman, R. L.; Jiang, H. Z. H.; Forse, A. C.; Lee, J.-H.; Martell, J. D.; Milner, P. J.; Falkowski, J. M.; Neaton, J. B.; Reimer, J. A.; Weston, S. C.; Long, J. R. Cooperative Carbon Capture and Steam Regeneration with Tetraamine-Appended Metal–Organic Frameworks. *Science* **2020**, *369* (6502), 392–396. https://doi.org/10.1126/science.abb3976.

(23) Granite, E. J.; Pennline, H. W. Photochemical Removal of Mercury from Flue Gas. *Ind. Eng. Chem. Res.* **2002**, *41* (22), 5470–5476. https://doi.org/10.1021/ie020251b.

(24) Forse, A. C.; Milner, P. J.; Lee, J.-H.; Redfearn, H. N.; Oktawiec, J.; Siegelman, R. L.; Martell, J. D.; Dinakar, B.; Porter-Zasada, L. B.; Gonzalez, M. I.; Neaton, J. B.; Long, J. R.; Reimer, J. A. Elucidating $CO_2$ Chemisorption in Diamine-Appended Metal–Organic Frameworks. *J. Am. Chem. Soc.* **2018**, *140* (51), 18016–18031. https://doi.org/10.1021/jacs.8b10203.

(25) Puibasset, J.; Kierlik, E.; Tarjus, G. Influence of Reservoir Size on the Adsorption Path in an Ideal Pore. *J. Chem. Phys.* **2009**, *131* (12), 124123. https://doi.org/10.1063/1.3236510.

(26) Martell, J. D.; Porter-Zasada, L. B.; Forse, A. C.; Siegelman, R. L.; Gonzalez, M. I.; Oktawiec, J.; Runčevski, T.; Xu, J.; Srebro-Hooper, M.; Milner, P. J.; Colwell, K. A.; Autschbach, J.; Reimer, J. A.; Long, J. R. Enantioselective Recognition of Ammonium Carbamates in a Chiral Metal–Organic Framework. *J. Am. Chem. Soc.* **2017**, *139* (44), 16000–16012. https://doi.org/10.1021/jacs.7b09983.

(27) Martell, J. D.; Milner, P. J.; Siegelman, R. L.; Long, J. R. Kinetics of Cooperative $CO_2$ Adsorption in Diamine-Appended

Variants of the Metal–Organic Framework $Mg_2$(dobpdc). *Chem. Sci.* **2020**. https://doi.org/10.1039/D0SC01087A.

(28) Lee, J.-H.; Siegelman, R. L.; Maserati, L.; Rangel, T.; Helms, B. A.; Long, J. R.; Neaton, J. B. Enhancement of $CO_2$ Binding and Mechanical Properties upon Diamine Functionalization of $M_2$(dobpdc) Metal–Organic Frameworks. *Chem. Sci.* **2018**, *9* (23), 5197–5206. https://doi.org/10.1039/C7SC05217K.

(29) Zhang, H.; Yang, L.-M.; Ganz, E. Adsorption Properties and Microscopic Mechanism of $CO_2$ Capture in 1,1-Dimethyl-1,2-Ethylenediamine-Grafted Metal–Organic Frameworks. *ACS Appl. Mater. Interfaces* **2020**, *12* (16), 18533–18540. https://doi.org/10.1021/acsami.0c01927.

(30) Perdew, J. P.; Burke, K.; Ernzerhof, M. Generalized Gradient Approximation Made Simple. *Phys. Rev. Lett.* **1996**, *77* (18), 3865–3868. https://doi.org/10.1103/PhysRevLett.77.3865.

(31) Grimme, S.; Ehrlich, S.; Goerigk, L. Effect of the Damping Function in Dispersion Corrected Density Functional Theory. *J. Comput. Chem.* **2011**, *32* (7), 1456–1465. https://doi.org/10.1002/jcc.21759.

(32) Hammer, B.; Hansen, L. B.; Nørskov, J. K. Improved Adsorption Energetics within Density-Functional Theory Using Revised Perdew-Burke-Ernzerhof Functionals. *Phys. Rev. B* **1999**, *59* (11), 7413–7421. https://doi.org/10.1103/PhysRevB.59.7413.

(33) Massiot, D.; Fayon, F.; Capron, M.; King, I.; Calvé, S. L.; Alonso, B.; Durand, J.-O.; Bujoli, B.; Gan, Z.; Hoatson, G. Modelling One- and Two-Dimensional Solid-State NMR Spectra. *Magn. Reson. Chem.* **2002**, *40* (1), 70–76. https://doi.org/10.1002/mrc.984.

(34) Bertani, P.; Raya, J.; Bechinger, B. $^{15}$N Chemical Shift Referencing in Solid State NMR. *Solid State Nucl. Magn. Reson.* **2014**, *61–62*, 15–18. https://doi.org/10.1016/j.ssnmr.2014.03.003.

(35) Blöchl, P. E. Projector Augmented-Wave Method. *Phys. Rev. B* **1994**, *50* (24), 17953–17979. https://doi.org/10.1103/PhysRevB.50.17953.

(36) Kresse, G.; Joubert, D. From Ultrasoft Pseudopotentials to the Projector Augmented-Wave Method. *Phys. Rev. B* **1999**, *59* (3), 1758–1775. https://doi.org/10.1103/PhysRevB.59.1758.

(37) Kresse, G.; Hafner, J. Ab Initio Molecular Dynamics for Liquid Metals. *Phys. Rev. B* **1993**, *47* (1), 558–561. https://doi.org/10.1103/PhysRevB.47.558.

(38) Kresse, G.; Furthmüller, J. Efficient Iterative Schemes for Ab Initio Total-Energy Calculations Using a Plane-Wave Basis Set. *Phys. Rev. B* **1996**, *54* (16), 11169–11186. https://doi.org/10.1103/PhysRevB.54.11169.

(39) Kresse, G.; Furthmüller, J. Efficiency of Ab-Initio Total Energy Calculations for Metals and Semiconductors Using a Plane-Wave Basis Set. *Comput. Mater. Sci.* **1996**, *6* (1), 15–50. https://doi.org/10.1016/0927-0256(96)00008-0.

(40) Kresse, G.; Hafner, J. Ab Initio Molecular-Dynamics Simulation of the Liquid-Metal--Amorphous-Semiconductor Transition in Germanium. *Phys. Rev. B* **1994**, *49* (20), 14251–14269. https://doi.org/10.1103/PhysRevB.49.14251.

(41) Pack, J. D.; Monkhorst, H. J. "Special Points for Brillouin-Zone Integrations"---a Reply. *Phys. Rev. B* **1977**, *16* (4), 1748–1749. https://doi.org/10.1103/PhysRevB.16.1748.

(42) Elsässer, C.; Fähnle, M.; Chan, C. T.; Ho, K. M. Density-Functional Energies and Forces with Gaussian-Broadened Fractional Occupations. *Phys. Rev. B* **1994**, *49* (19), 13975–13978. https://doi.org/10.1103/PhysRevB.49.13975.

(43) Baias, M.; Widdifield, C. M.; Dumez, J.-N.; Thompson, H. P. G.; Cooper, T. G.; Salager, E.; Bassil, S.; Stein, R. S.; Lesage, A.; Day, G. M.; Emsley, L. Powder Crystallography of Pharmaceutical Materials by Combined Crystal Structure Prediction and Solid-State $^{1}$H NMR Spectroscopy. *Phys. Chem. Chem. Phys.* **2013**, *15* (21), 8069–8080. https://doi.org/10.1039/C3CP41095A.

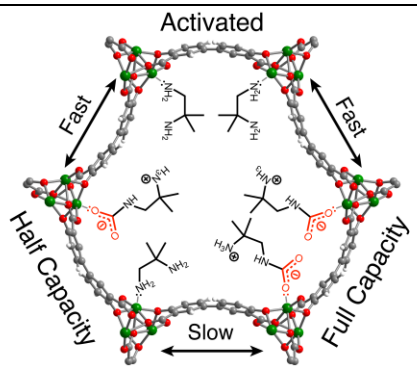
Activated
Fast
Fast
Half Capacity
Full Capacity
Slow